



# Responses of global monsoon and seasonal cycle of precipitation to precession and obliquity forcing

Zhaomin Ding<sup>1,3,4</sup> · Gang Huang<sup>1,2,4</sup> · Fei Liu<sup>5,7</sup> · Renguang Wu<sup>1,6</sup> · Pengfei Wang<sup>1,3</sup>

Received: 28 August 2020 / Accepted: 18 January 2021 / Published online: 1 February 2021  
© The Author(s), under exclusive licence to Springer-Verlag GmbH, DE part of Springer Nature 2021

## Abstract

In this paper, the response of global monsoon to changes in orbital forcing is investigated using a coupled atmosphere–ocean general circulation model with an emphasis on relative roles of precession and obliquity changes. When precession decreases, there are inter-hemispheric asymmetric responses in monsoonal precipitation, featuring a significant increase over most parts of the Northern Hemisphere (NH) monsoon regions and a decrease over the Southern Hemisphere (SH) monsoon regions. In contrast, when obliquity increases, global monsoon is enhanced except for the American monsoon. Dynamic effects (caused by changes in winds with humidity unchanged) dominate the monsoonal precipitation response to both precession and obliquity forcing, while thermodynamic effects (caused by changes in humidity with winds unchanged) is related to the northward extension of the North African summer monsoon. During minimum precession, the seasonal cycle of tropical precipitation is advanced with respect to the maximum precession. The rainfall increase in the transitional season (April–June in the NH and October–December in the SH) is dominated by the dynamic component. From an energetics perspective, the southward (northward) cross-equatorial energy transport during April–June (October–December) corresponds to a northward (southward) shift of tropical precipitation, which results in a seasonal advance in the migration of tropical precipitation. Nonetheless, there is no significant change in the seasonal cycle in response to obliquity forcing.

**Keywords** Precession · Obliquity · Global monsoon · Seasonal cycle

✉ Gang Huang  
hg@mail.iap.ac.cn

- <sup>1</sup> State Key Laboratory of Numerical Modeling for Atmospheric Sciences and Geophysical Fluid Dynamics, Institute of Atmospheric Physics, Chinese Academy of Sciences, 40 Hua Yan Li, Beijing 100029, China
- <sup>2</sup> Laboratory for Regional Oceanography and Numerical Modeling, Qingdao National Laboratory for Marine Science and Technology, Qingdao, China
- <sup>3</sup> Center for Monsoon System Research, Institute of Atmospheric Physics, Chinese Academy of Sciences, Beijing, China
- <sup>4</sup> College of Earth and Planetary Sciences, University of Chinese Academy of Sciences, Beijing, China
- <sup>5</sup> School of Atmospheric Sciences, Sun Yat-Sen University, Zhuhai, China
- <sup>6</sup> School of Earth Sciences, Zhejiang University, Hangzhou, China
- <sup>7</sup> Southern Marine Science and Engineering Guangdong Laboratory, Zhuhai, China

## 1 Introduction

Monsoon climates have undergone striking changes during the geological past. On the Milankovith time scale, changes in orbital parameters (precession, obliquity and eccentricity) influence the distribution of incoming solar radiation at the top of the atmosphere (Berger 1978). Earth's axial and apsidal precession modulates the seasonal distribution of insolation with a periodicity of about 23 kyr (Berger 1978). The insolation changes induced by obliquity, the tilt of the Earth's rotational axis, are small at low latitudes, yet proxy climate records from tropical and subtropical regions reveal a clear obliquity signal (Caley et al. 2011; Clemens et al. 2010).

Paleoclimate records suggest significant changes in regional monsoons during the Holocene (Gupta et al. 2006; Pokras and Mix 1987). Lake status and pollen records show much wetter conditions in North Africa in the early Holocene (Kohfeld and Harrison 2000). The deposition of successive sapropels in the Mediterranean Sea showed strong signals of precession in the African

monsoon (Rossignol-Strick 1983). Alternating thick/thin sapropels in the Mediterranean Sea also reflect a prominent obliquity component (Lourens et al. 2001). Continental loess and deep-sea records showed that the Asian summer monsoon is sensitive to orbital forcing in terms of precession and obliquity periods (Liu et al. 1999). Pollen records indicated the importance of both precession and obliquity in driving the Australian monsoon (Kershaw et al. 2003).

Numerous modeling studies have been conducted to evaluate the response of monsoon to astronomical forcing (e.g., Caley et al. 2014; Chen et al. 2011; Kutzbach et al. 2008; Liu et al. 2003, 2006; Prell and Kutz 1987; Shi et al. 2011, 2012; Weber and Tuenter 2011). A large number of these studies, however, considered the combined effects of precession and obliquity on the insolation forcing. Few modeling studies separated the precession and obliquity signals (Bosmans et al. 2015a, b, 2018; Erb et al. 2013; Lee et al. 2019; Mantsis et al. 2013; Tuenter et al. 2003; Wu et al. 2016; Wyrwoll et al. 2007). Tuenter et al. (2003) suggested that the African summer monsoon is influenced by both precession and obliquity, and the amplitude of the precipitation response to precession change is independent of that to obliquity change, while the obliquity signal depends on the prevailing precession. Wyrwoll et al. (2007) showed that in spite of a weaker summer insolation forcing over the Australian continent for obliquity than for precession, the enhanced Australian summer monsoon rainfall is almost comparable, while the modulation of obliquity on the precession effect and the modulation of precession on the obliquity effect are both small. Mantsis et al. (2013) investigated the precession influences on the Northern Hemisphere (NH) summer anticyclones, and identified enhanced precipitation over the monsoon regions at times of increased NH summer insolation. Using idealized aqua-planet simulations, Merlis et al. (2013a, b) showed that more precipitation occurs in the summer with perihelion, and identified a poleward shift in monsoonal precipitation over an idealized subtropical continent. Bosmans et al. (2015a) found that increased moisture transport from tropical Atlantic is responsible for the precession and obliquity signals in the North African monsoon, and the increased moisture transport results from an increased tropical insolation gradient.

Previous studies generally focus on the response of summer monsoon intensity to orbital change. However, little is known about changes in the seasonal cycle of tropical precipitation in response to respective precession and obliquity forcing. Based on studies using an atmospheric general circulation model, Shi et al. (2016) showed that the withdrawals of rainy seasons in northern East Asia and the India-Bay of Bengal region are sensitive, while the onsets

are less sensitive to precession variation under interglacial-like conditions.

In this study, we used a coupled atmosphere–ocean general circulation model to investigate both precession and obliquity signals in the global monsoon using an extensive set of orbital parameters. This paper is organized as follows. Section 2 describes data, methods, and the model, evaluates the model performance, and outlines the model experiments. In Sects. 3 and 4, we explore global monsoon responses in the model experiments, including monsoonal precipitation changes (Sect. 3) and seasonal cycle changes (Sect. 4). Conclusions and discussion are given in Sect. 5.

## 2 Data, methods, model, and model evaluation and experiments

### 2.1 Data

The precipitation from the Climate Prediction Center (CPC) Merged Analysis of Precipitation (CMAP) dataset (Xie and Arkin 1997) is used as a proxy of observations. The spatial resolution of the CMAP is 2.5° latitude and 2.5° longitude. The temporal coverage of the CMAP starts from 1979 to the present.

### 2.2 Methods

The simple metrics proposed by Wang and Ding (2008) are used in evaluation of model's performance in simulating precipitation climatology in this paper. They include annual-mean precipitation, the first and second modes of annual variation of precipitation, and annual range of precipitation (local summer minus winter mean) and domain. Here, local summer refers to May through September for the NH and November through March for the Southern Hemisphere (SH), and vice versa. The first mode represents a solstice global monsoon mode, and can be captured by June–September minus December–March mean precipitation (Wang and Ding 2008). The second mode represents a spring–fall asymmetric mode, and its spatial pattern can be captured by April–May minus October–November mean precipitation. The global monsoon precipitation domain is identified as the regions where the annual range of precipitation exceeds 2.0 mm/day, and local summer precipitation exceeds 55% of the annual total (Wang et al. 2012).

To understand the relative roles of thermodynamic and dynamical factors on the rainfall changes, we conducted a moisture budget analysis based on the linearized formulation used by Chou et al. (2009) as follows:

$$\Delta P = \frac{1}{\rho_w g} \left( - \int_0^{p_s} \bar{\omega} \frac{\partial \Delta q}{\partial p} - \int_0^{p_s} \Delta \omega \frac{\partial \bar{q}}{\partial p} - \Delta \left( \int_0^{p_s} \mathbf{V} \Delta \nabla q \right) \right) + \Delta E + residual, \tag{1}$$

where  $P$ ,  $\rho_w$ ,  $g$ ,  $\omega$ ,  $p$ ,  $q$ ,  $\mathbf{V}$ , and  $E$  represent precipitation, the density of water, the acceleration due to gravity, pressure velocity, pressure, specific humidity, vector horizontal wind, and evaporation, respectively. The subscript ‘ $s$ ’ denotes surface values. Overbars indicate climatology in the reference simulation with perihelion in December (or minimum obliquity), and  $\Delta$  indicate the difference between simulations with perihelion in June and December (or maximum obliquity and minimum obliquity). The first three terms on the right-hand side of Eq. (1) denote the thermodynamic, dynamic and horizontal moisture advection terms, respectively. The residual term includes mainly the nonlinear terms and transient eddy, which are negligible.

We explore the shift of tropical precipitation from an energetics perspective following Song et al. (2018a). According to the atmospheric energy equation (Neelin and Held 1987), the divergence of atmospheric energy transport equals to the difference between net input energy and the tendency of the moist static energy:

$$\nabla \cdot \mathbf{E} = F_{net} - \frac{\partial h}{\partial t} \tag{2}$$

where  $E$  denotes atmospheric energy transport,  $F_{net}$  is net energy input to the atmosphere,  $h$  is moist static energy,  $t$  is time, and  $\langle \rangle$  represents vertical integral from the surface to the top of the model.

$$F_{net} = S_t^\downarrow - S_t^\uparrow - R_t^\uparrow - S_s^\downarrow + S_s^\uparrow - R_s^\downarrow + R_s^\uparrow + LH + SH \tag{3}$$

where subscripts  $s$  and  $t$  denote surface and model top,  $S$  is solar radiation,  $R$  is longwave radiation,  $LH$  is latent heat flux, and  $SH$  is sensible heat flux.

$$h = c_p T + gz + L_v q. \tag{4}$$

Here,  $c_p$ ,  $T$ ,  $g$ ,  $z$ ,  $L_v$  and  $q$  represent specific heat at constant pressure, air temperature, acceleration due to gravity, geopotential height, latent heat of vaporization and specific humidity, respectively.

### 2.3 Model, model evaluation and model experiments

The model used is the Integrated Climate Model (ICM), a fully coupled atmosphere–ocean general circulation model without flux corrections (Huang et al. 2014). The atmospheric component of ICM is the Hamburg Atmospheric General Circulation Model Version 5 (ECHAM5) (Roeckner

et al. 2003). Its spectral horizontal resolution is T31 (roughly  $3.75^\circ$  by  $3.75^\circ$ ) with 19 vertical levels. The ocean component consists of the Nucleus for European Modeling of the Ocean Version 2.3 (NEMO 2.3) (Madec 2008), running with a horizontal grid resolution of 182 (longitude)  $\times$  149 (latitude) ( $\sim 2^\circ$  at high latitudes and a finer meridional resolution of  $0.5^\circ$  in the tropics). There are 31 vertical levels in the ocean to a depth of 5250.23 m, with 10 levels in the top 100 m. NEMO includes the Louvain-la-Neuve Ice Model Vtropicsersion 2 (LIM2) sea ice model. The atmosphere, ocean and sea-ice are coupled through the Ocean Atmosphere Sea Ice Soil Version 3 (OASIS3) (Valcke 2006).

ICM performs well for the present-day mean climate compared to observations (Huang et al. 2014; Liu et al. 2017). In particular, it has been shown that monsoonal precipitation is represented reasonably in ICM. The model evaluation is based on the last millennium transient simulation of ICM driven by up-to-date external forcing from 850 to 2000. Detailed information about the simulation can be found in Ding et al. (2017). As shown in Fig. 1, both the magnitude and spatial pattern of annual-mean precipitation, the first and second modes of annual variation of precipitation are simulated quite well compared to the CMAP precipitation. ICM captures the major regional summer monsoon domains and annual range of precipitation realistically though biases exist over the western North Pacific monsoon region (Fig. 2). The pattern correlation coefficient between simulated and observed annual range of precipitation is 0.74.

To explore the respective precession and obliquity signals in the global monsoon, six idealized equilibrium simulations with different orbital parameters have been conducted:

- (1) PLTH: minimum precession with maximum obliquity
- (2) PHTH: maximum precession with maximum obliquity
- (3) PLTL: minimum precession with minimum obliquity
- (4) PHTL: maximum precession with minimum obliquity
- (5) POTH: maximum obliquity with a circular orbit
- (6) POTL: minimum obliquity with a circular orbit

The values of the orbital configurations are given in Table 1. These are similar to the experiments in Tuentner et al. (2003) except that we took extreme values of orbital parameters in the past 600 kyr (Berger 1978). For precession, extreme values of the precession parameter  $e \sin(\pi + \tilde{\omega})$  rather than extreme values of  $\tilde{\omega}$  are chosen as precession is modulated by eccentricity  $e$ .  $\tilde{\omega}$  is the longitude of perihelion, defined as the angle between the vernal equinox and

**Fig. 1** Comparison of precipitation climatology between model simulation (1979–2000; left panels) and CMAP observation (1979–2008, right panels). **a** Annual-mean precipitation rate, **c** the first annual cycle mode (solstice mode), and **e** the second annual cycle mode (spring-fall asymmetric mode)

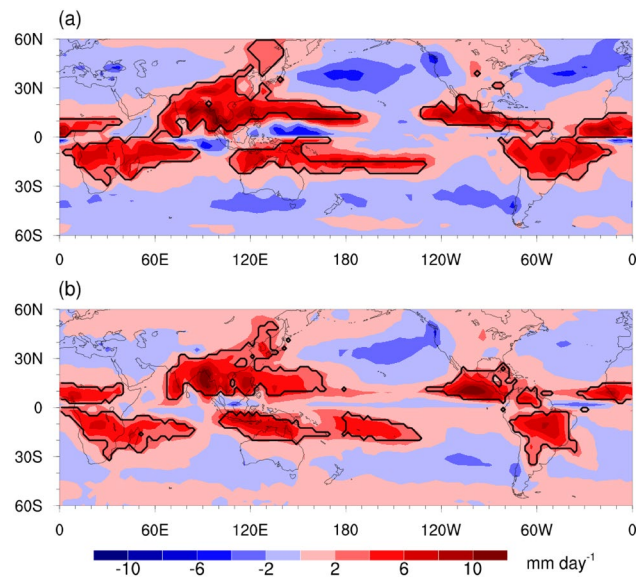
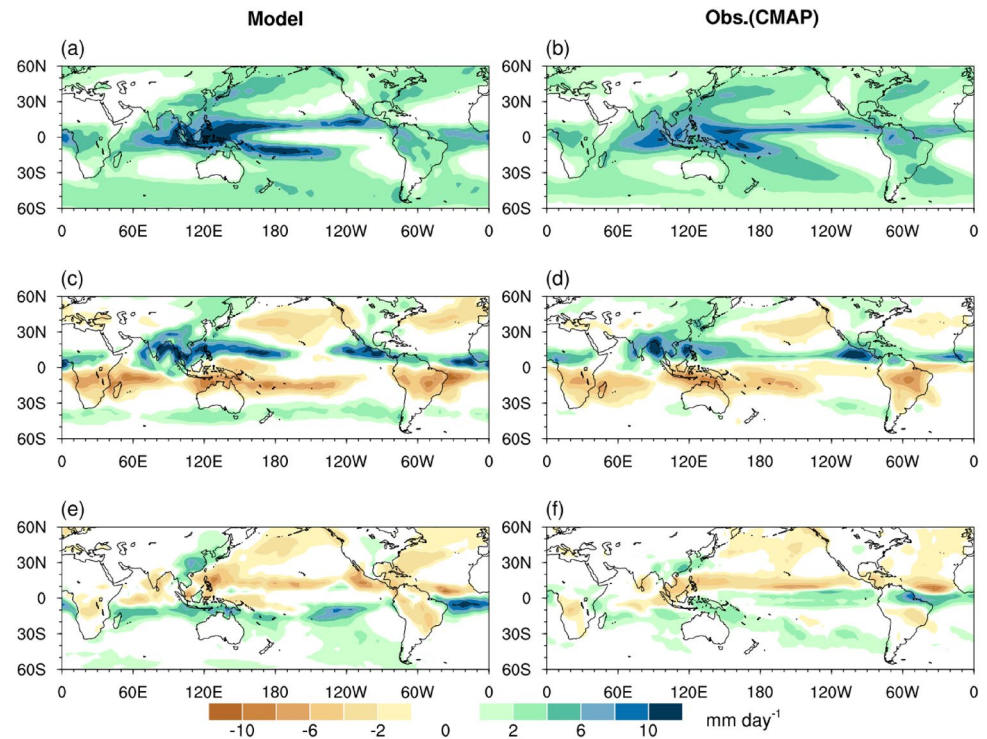


**Fig. 2** Annual range of precipitation and the global monsoon domain (outlined by black contour). **a** Model simulation (1979–2000) and **b** CMAP observation (1979–2008)

perihelion (measured counterclockwise). During a precession minimum (maximum), perihelion occurs at northern (southern) summer solstice, referred to as June (December) perihelion for brevity.

Each experiment was integrated for a period of 500 years, initialized from a preindustrial control

**Table 1** The orbital configurations in the six sensitivity experiments

Experiment	$e$	Tilt ( $^{\circ}$ )	$\tilde{\omega}$ ( $^{\circ}$ )	$e \sin(\pi + \tilde{\omega})$
PLTH	0.049	24.5	90	-0.049
PHTH	0.049	24.5	270	0.049
PLTL	0.049	22.1	90	-0.049
PHTL	0.049	22.1	270	0.049
P0TH	0	24.5	-	0
P0TL	0	22.1	-	0

PH and PL represent maximum and minimum precession, respectively. TH and TL are maximum and minimum tilt, respectively. The maximum (minimum) precession means winter (summer) solstice in perihelion. P0 represents a circular Earth orbit.  $e$  is eccentricity,  $\omega$  is the longitude of perihelion, defined as the angle between the vernal equinox and perihelion (measured counterclockwise)

simulation of ICM. The first 300 years of the simulations are considered spin-up, and the last 200 years are used to obtain monthly mean annual cycles. The orbital parameters were kept constant during the simulations. All other variables, such as greenhouse gas concentration and surface boundary conditions, were held at the preindustrial levels. We use the present-day calendar with a fixed vernal equinox at March 21st. This introduces some errors in the precession experiments (PLTH, PHTH, PLTL and PHTL) as the lengths of seasons and dates of equinoxes and solstices depend on the longitude of the perihelion according to Kepler's second law (Joussaume and Braconnot 1997).



In the precession results, a calendar conversion has been made following Pollard and Reusch (2002). However, because the calendar-effect only has minor effects on our results, the results of celestial longitude averages are not presented here.

In this paper, we will mainly discuss the precession signal with a maximum obliquity and the obliquity signal with a circular Earth orbit. The latter fully exclude precession in the obliquity experiments as there is no influence of precession during a circular Earth orbit. The other experiments will not be presented unless there are significant differences.

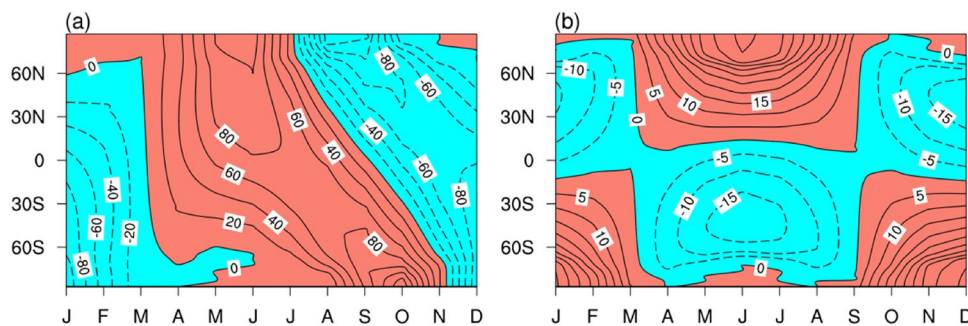
### 3 The monsoonal precipitation changes

In this section, we investigate the changes in monsoonal precipitation induced by precession and obliquity forcing and the contributions of different processes. We present the differences between minimum and maximum precession, and maximum and minimum obliquity.

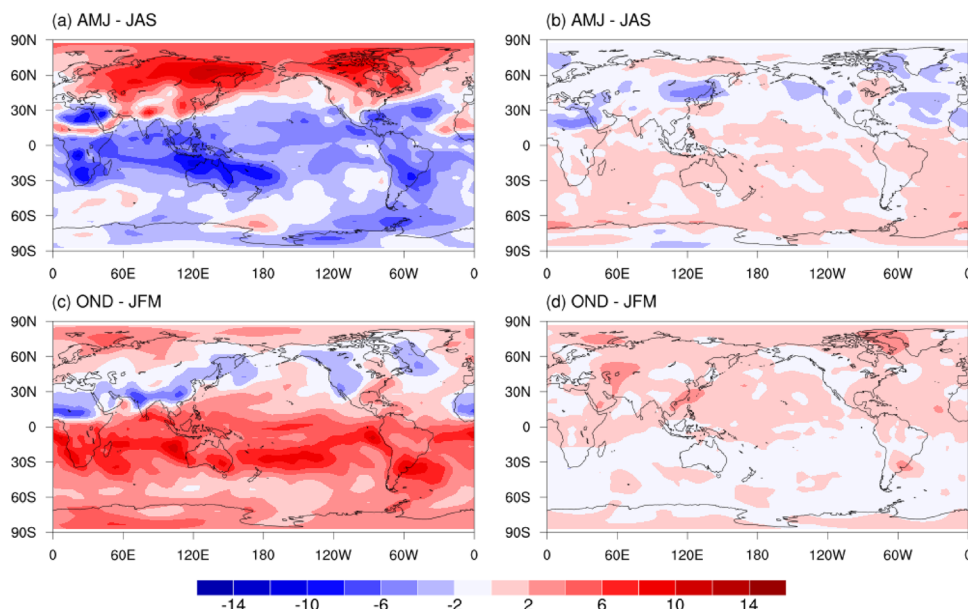
Figure 3 shows the changes in incoming solar radiation at the top of the atmosphere caused by precession and obliquity changes. Insolation in boreal summer is larger during the minimum precession than during the maximum precession, while insolation in austral summer is smaller during the minimum precession than during the maximum precession, with the differences as much as about  $90 \text{ W/m}^2$  (Fig. 3a). This means that seasonal cycle is enhanced in the NH and reduced in the SH during the minimum precession. During an obliquity maximum, the insolation is increased during both NH and SH summers, especially over the high latitudes, whereas the obliquity-induced insolation changes are small over the tropics during summers ( $< 5 \text{ W/m}^2$ ) (Fig. 3b).

As shown in Fig. 3a, when perihelion processes from December to June, the change in incoming shortwave radiation in the NH is much larger than that in the SH during boreal spring. The seasonal difference of 925-hPa equivalent potential temperature  $\theta_e$  between April–June (AMJ) and July–September (JAS) for PLTH minus PHTH displays a interhemispheric contrast (Fig. 4a). More energy in the NH

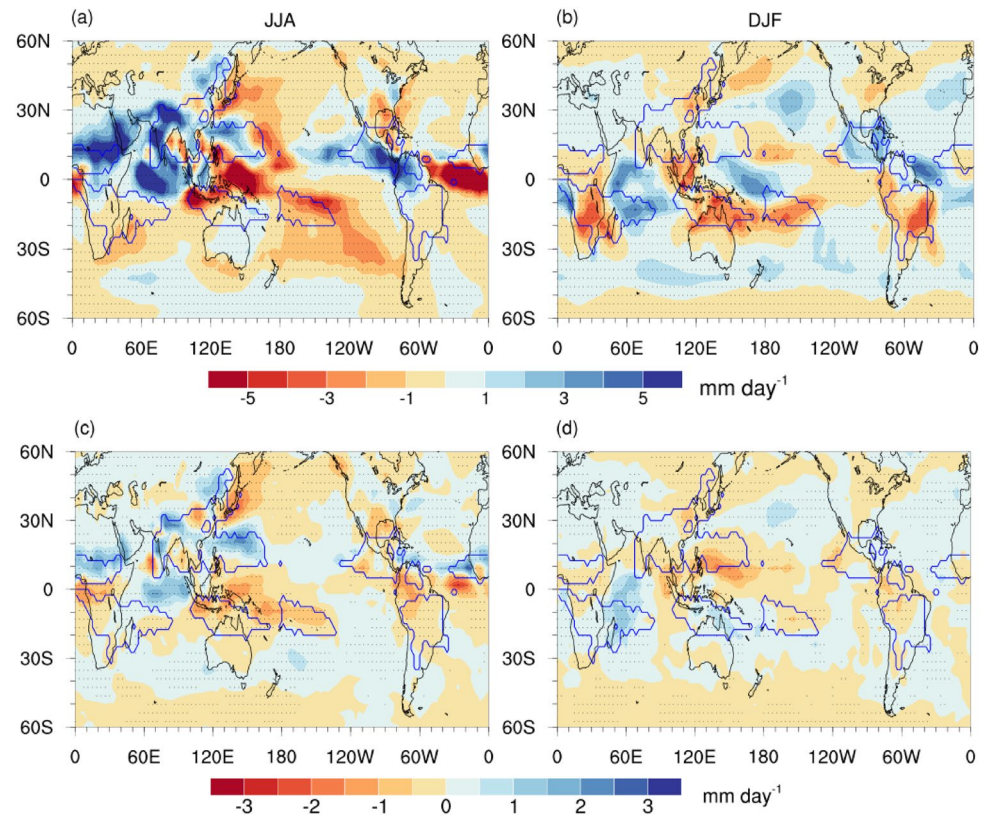
**Fig. 3** Monthly differences of incoming insolation at the top of the atmosphere ( $\text{W/m}^2$ ). **a** PLTH–PHTH, **b** POTH–POTL



**Fig. 4** Seasonal differences of 925-hPa equivalent potential temperature (K) between AMJ and JAS for **a** PLTH–PHTH, and **b** POTH–POTL. **c** and **d** Same as **a** and **b** but for differences between OND and JFM



**Fig. 5** Seasonal differences of precipitation. **a** PLTH–PHTH during JJA, **b** PLTH–PHTH during DJF, **c** POTH–POTL during JJA and **d** POTH–POTL during DJF. Stippled areas are significant at the 95% confidence level based on Student's *t* test. Monsoon domain (blue contour) is defined in Fig. 2b



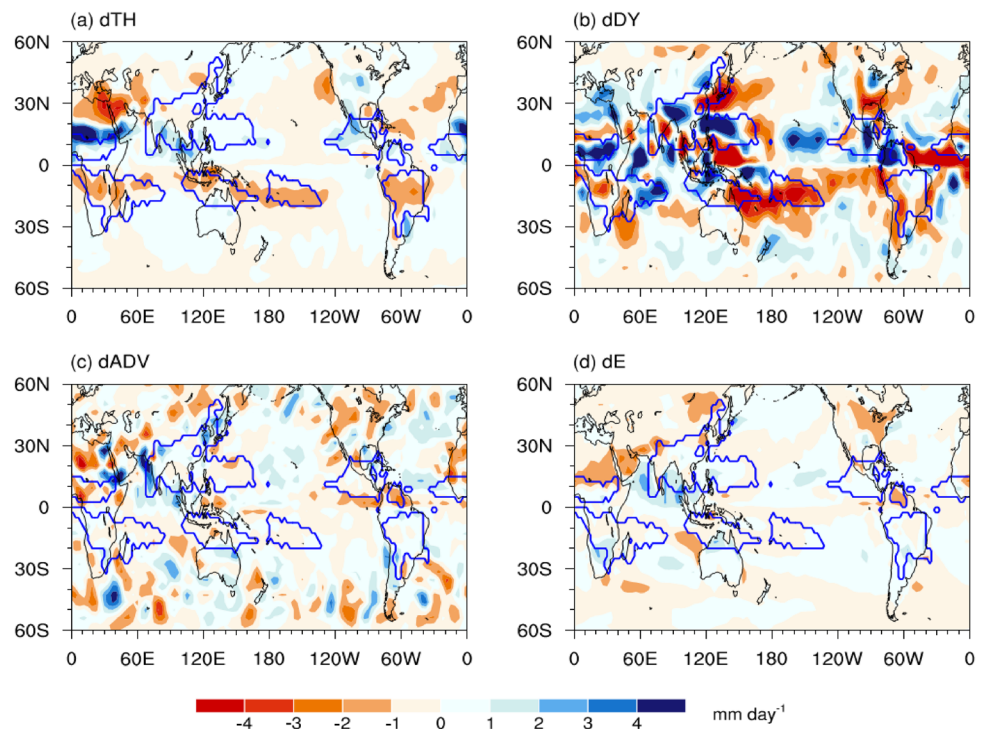
during the transition season (AMJ) under precession forcing engenders cross-equatorial energy transport. Hence, one should generally expect a seasonal advance in the migration of tropical precipitation from the SH to the NH (Song et al. 2018b), which will be discussed in Sect. 4. This energy contrast is also evident between October–December (OND) and January–March (JFM) (Fig. 4c). Under obliquity forcing, however, there is no clear interhemispheric contrast in the interseasonal  $\theta_e$  difference (Fig. 4b, d).

Figure 5a and b show precipitation differences between PLTH and PHTH in June–August (JJA) and December–February (DJF). During boreal summer, precipitation is enhanced over the North African, Asian and North American monsoon regions (Fig. 5a). And a remarkable decrease is seen over the western equatorial Pacific and tropical Atlantic Ocean. During austral summer, precipitation is reduced over land parts of the South African, Australian and South American monsoon regions, while more precipitation occurs over the oceans (Fig. 5b). Changes in precipitation due to changes in precession are similar whether obliquity is set to minimum or maximum values (not shown). Interhemispheric contrast in the global monsoon at precessional timescales is a robust feature of proxy reconstructions, which show an anti-phased relationship between hemispheres (Cheng et al. 2012a; Wang et al. 2014). The northward expansion and stronger sensitivity of the North African monsoon in

simulations is in concert with proxy records (deMenocal et al. 2000; Joussaume et al. 1999).

Figure 5c and d show the precipitation differences between POTH and POTL. Although the obliquity-induced insolation changes are small over the tropics during summers, there is a clear response of monsoonal precipitation. The JJA precipitation increases significantly over the Asian and North African monsoon regions, whereas it decreases over the North American monsoon region (Fig. 5c). During austral summer, rainfall is reduced over the South American monsoon region, opposite to the increased rainfall over the South African and Australian monsoon regions (Fig. 5d). It is noted that the response in the Australian monsoon is much smaller than the results in Wyrwoll et al. (2007). The obliquity signal is similar when precession is set to maximum values or to a circular Earth orbit. During minimum precession, the response in the Asian and North African monsoon is weaker than in the other experiments, whereas the response in the North American monsoon is stronger (not shown). Tuenter et al. (2003) suggested that during minimum precession, the obliquity forcing is added to a larger insolation in boreal spring and summer than during maximum precession and a circular Earth orbit, which results in low soil moisture and thus a limited humidity supply for the large-scale circulation. However, the reason for the enhanced North American monsoon warrants further investigation. Paleoclimate data indicate that strong summer monsoons occur

**Fig. 6** Differences in the moisture budget for the summer season between PLTH and PHTH. Shown are **a** thermodynamic (dTH), **b** dynamic (dDY), **c** horizontal moisture advection (dADV), and **d** evaporation (dE) terms. Monsoon domain (blue contour) is defined in Fig. 2b



at obliquity maximum despite weak variations in incoming solar radiation at low latitudes (Caley et al. 2011; Clemens et al. 2010; Mohtadi et al. 2016).

Figure 6 presents the spatial patterns of changes in the four terms on the right-hand side of Eq. (1) during the summer season (JJA for the NH and DJF for the SH) between PLTH and PHTH. Compared with the precipitation differences between June and December perihelion (Fig. 5a, b), it is evident that the precipitation changes are mostly dominated by the dynamic component (Fig. 6b). Both the pattern and magnitude of the dynamic term correspond well with the precession-induced precipitation changes. Comprehensive general circulation model (GCM) experiments have detected both strengthening and weakening of the cross-equatorial Hadley circulation in NH summer in response to perihelion variations (Clement et al. 2004; Khon et al. 2010). Ashkenazy et al. (2010) showed little change in the strength of the Hadley circulation in response to changes in precession. Merlis et al. (2013a, b) suggested that the different circulation responses to orbital precession are due to the differences in model formulation. Clement et al. (2004) and Hsu et al. (2010) found that the dynamic changes dominate the hemispherically antisymmetric monsoonal precipitation response to precession.

However, there is a significant contribution to the moisture balance by the thermodynamic component (Fig. 6a). It is noticed that the northward extension of the North African summer monsoon rainband is associated with thermodynamic effect. The sign of thermodynamic term in the

monsoon region is consistent with that of specific humidity changes (not shown). The horizontal moisture advection and evaporation terms (Fig. 6c and d) generally have a more disorderly pattern with a small magnitude.

Figure 7 shows the changes in the four terms between POTH and POTL. The obliquity-induced monsoonal precipitation changes are also dominated by the dynamic component (Fig. 7b). The northward extension of the North African summer monsoon rainband is related to thermodynamic effect (Fig. 7a). The horizontal moisture advection and evaporation terms generally show a small magnitude in the monsoon regions (Fig. 7c and d). When obliquity is high, a stronger interhemispheric insolation gradient induces a stronger winter Hadley circulation (Bosmans et al. 2015a; Mantsis et al. 2014).

## 4 The seasonal cycle changes

In this section, we investigate the seasonal cycle changes induced by precession and obliquity forcing and the contributions of different processes and explore the changes from the energetics perspective. We present the differences between minimum and maximum precession, and maximum and minimum obliquity.

Figure 8 depicts the changes in seasonal cycle of monthly precipitation under orbital forcing. The northern tropics ( $0^{\circ}$ – $25^{\circ}$ N) receives more precipitation almost for the entire year except for October–December, but the opposite occurs



**Fig. 7** Same as Fig. 6 but for differences between P0TH and POTL

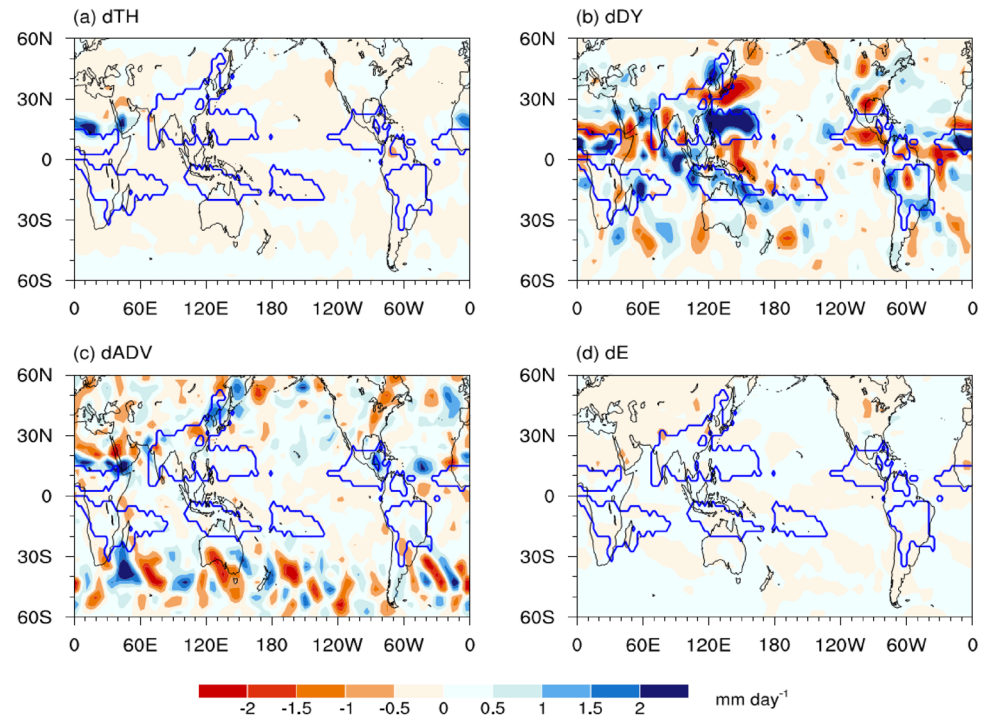
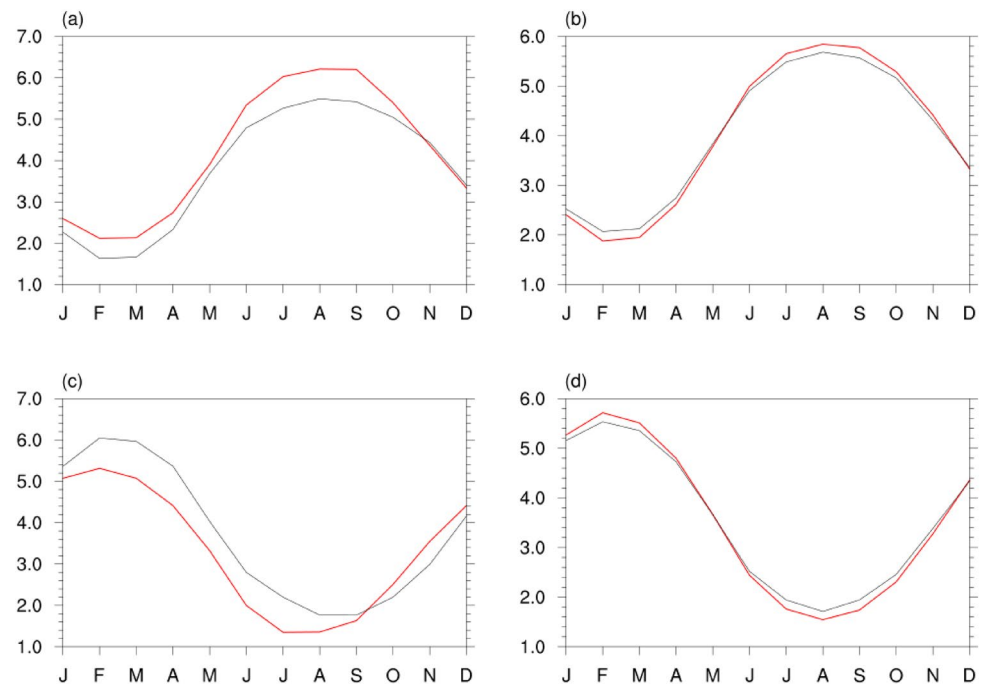


**Fig. 8** Climatology of monthly mean precipitation (mm/day) averaged over **a** the northern tropics ( $0^{\circ}$ – $25^{\circ}$ N) and **c** the southern tropics ( $0^{\circ}$ – $25^{\circ}$ S) based on PLTH (red line) and PHTH (black line). **b** and **d** Same as **a** and **c** but for P0TH (red line) and POTL (black line)



over the southern tropics ( $0^{\circ}$ – $25^{\circ}$ S) when perihelion changes from December to June (Fig. 8a and c). Summer precipitation is only slightly higher during maximum obliquity over both northern and southern tropics (Fig. 8b and d).

To further investigate the change in the seasonal cycle of precipitation, an empirical orthogonal function (EOF) analysis is applied to climatological monthly precipitation. Figure 9a shows the first EOF mode of seasonal variation

of precipitation in PHTH, which accounts for 63.6% of the total variance. The spatial pattern of EOF1 of precipitation depicts the shift of rainfall to the summer hemisphere (Biasutti and Sobel 2009). The June–December perihelion difference in corresponding principal component (PC1) suggests a phase shift in the seasonal evolution of rainfall in response to precession variations (Fig. 9c). Following Biasutti and Sobel (2009), we fit PC1 in December and June perihelion



**Fig. 9** The spatial patterns of EOF1 of **a** precipitation and **b** SST annual cycle in PHTH and the corresponding normalized PC1 of **c** precipitation and **d** SST in PHTH (black line) and the corresponding differences between PLTH and PHTH

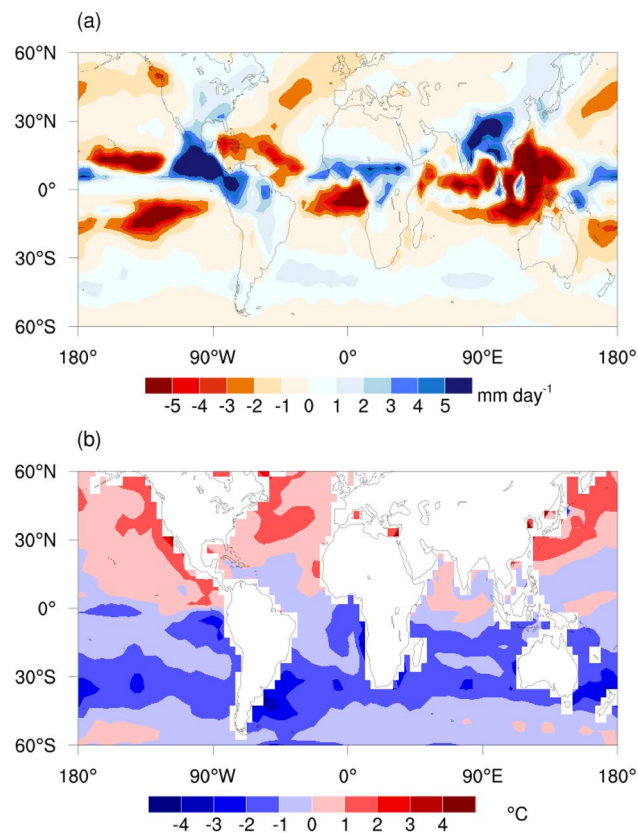
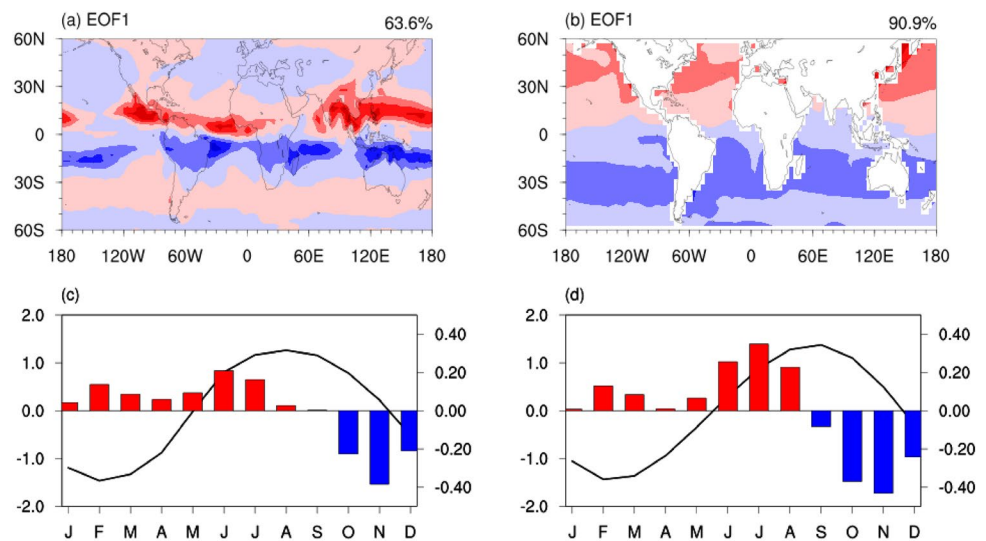


**Fig. 10** **a** May–October differences in precipitation PLTH-PHTH anomalies. **b** May–November differences in SST PLTH-PHTH anomalies

simulations to sinusoids ( $\sin(\theta)$  and  $\sin(\theta + \epsilon)$ , respectively). The shift  $\epsilon$  is estimated as 6.3 days, indicating an advance in the global annual cycle under the precession minimum. We also estimate the times when PC1 crosses the zero line in spring and autumn to quantify the change in the duration

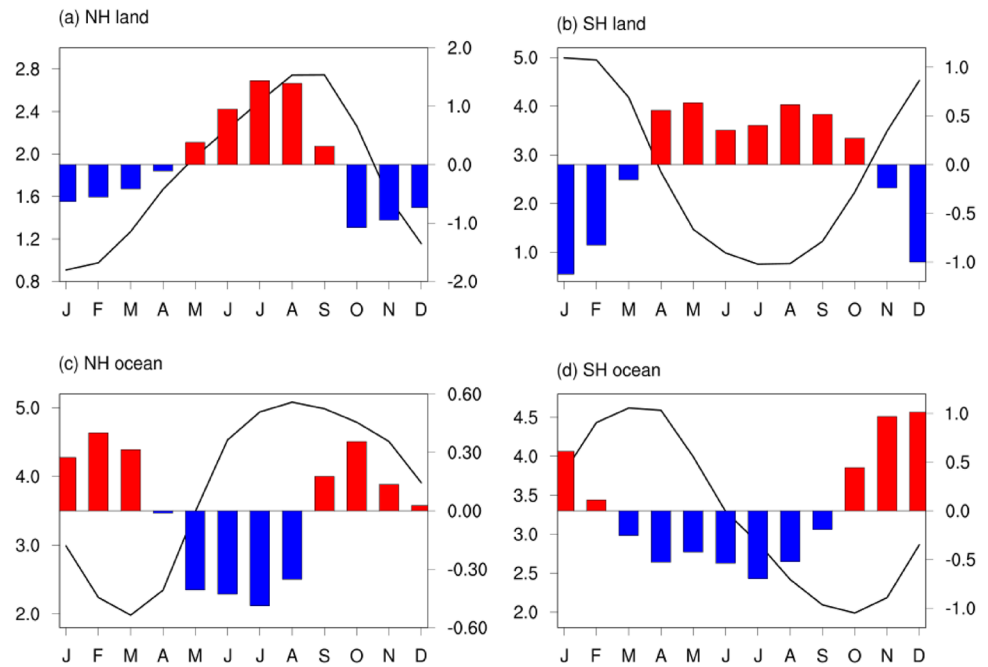
of the seasons. PC1 of precipitation crosses the zero line with a 3.2-day advance in spring and a 15.9-day advance in autumn, indicating that the NH summer becomes shorter by 12.7 days.

If May precipitation increases more than October precipitation when perihelion processes from December to June, it suggests an advance in the seasonal cycle in the NH. In Fig. 10a, the PLTH-PHTH difference in precipitation is obtained for May, then the same difference is obtained for October and subtracted from the May result. The results indicate an earlier advancement of precipitation into the NH over Asian, North African and North American monsoon regions. A similar result is obtained using the method in Song et al. (2018a) (not shown). Shi et al. (2016) evaluated the response of monsoon duration to orbital forcing, and found that the onset dates do not change significantly in response to the precession variations over the Asian monsoon region under interglacial-like condition. However, the withdrawal of rainy season is advanced over South Asia and northern East Asia when perihelion varies from December to June.

The leading mode of sea surface temperature (SST) in PHTH explains 90.9% of variance, characterized by large loading at the high latitudes and smaller loading at the tropics (Fig. 9b). We also check the phase change of SST (Fig. 9d), and the shift  $\epsilon$  is quantified as 8.1 days. PC1 of SST crosses the zero line with a 6.1- and 15.8-days advance in spring and autumn, respectively. In addition, most of the NH SST warms in May more than November (Fig. 10b). The consistent changes in seasonal cycle of global SST and rainfall suggest the advance in the seasonal cycle of SST may contribute to the advance in the seasonal cycle of global precipitation.

However, the phase changes of precipitation are different between land and ocean under the precession minimum.

**Fig. 11** The annual cycle of precipitation (mm/day) in PHTH (black line) and the differences between PLTH and PHTH over **a** NH land ( $0^{\circ}$ – $40^{\circ}$ N), **b** SH land ( $0^{\circ}$ – $40^{\circ}$ S), **c** NH ocean ( $0^{\circ}$ – $40^{\circ}$ N), and **d** SH ocean ( $0^{\circ}$ – $40^{\circ}$ S). For the differences between PLTH and PHTH, annual-mean changes are removed



Here, we examine the tropical and subtropical regions ( $40^{\circ}$ S– $40^{\circ}$ N) to include most land monsoon systems (Seth et al. 2013; Song et al. 2020), and similar results are obtained in the tropics ( $25^{\circ}$ S– $25^{\circ}$ N) (not shown). Over land, the precipitation difference in the NH reaches the largest earlier than the climatological peak in PHTH, while the SH mainly receives less rain during wet season and more rain during dry season, featuring a decreased amplitude of precipitation annual cycle (Fig. 11a, b). The distinct weakened annual cycle of SH land precipitation is consistent with the change in incoming solar radiation under the precession minimum (Fig. 3a). By removing the seasonal cycle in PHTH from the

SH land precipitation changes between PLTH and PHTH following Song et al. (2018a), the seasonality change is diminished. Over ocean, the NH phase is delayed and the SH phase is advanced in response to precession forcing (Fig. 11c, d).

Under global warming due to increasing greenhouse gases, the annual cycle of tropical precipitation is projected to be delayed (Biasutti and Sobel 2009; Dwyer et al. 2014). Meanwhile, a difference was reported between land and ocean in the phase change of the tropical precipitation annual cycle under warming, with a robust delay over land

**Fig. 12** Same as Fig. 9 but for POTH and POTL

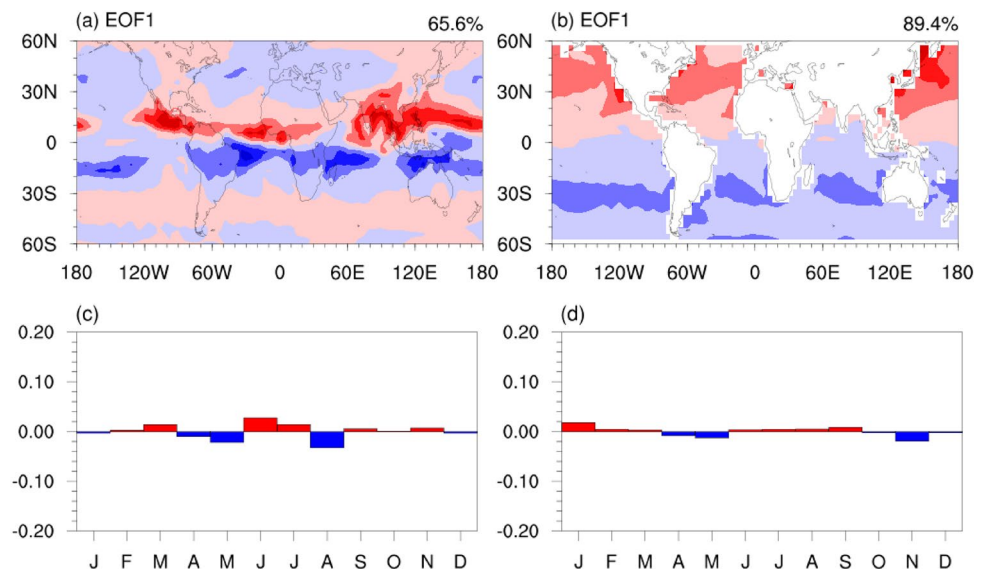
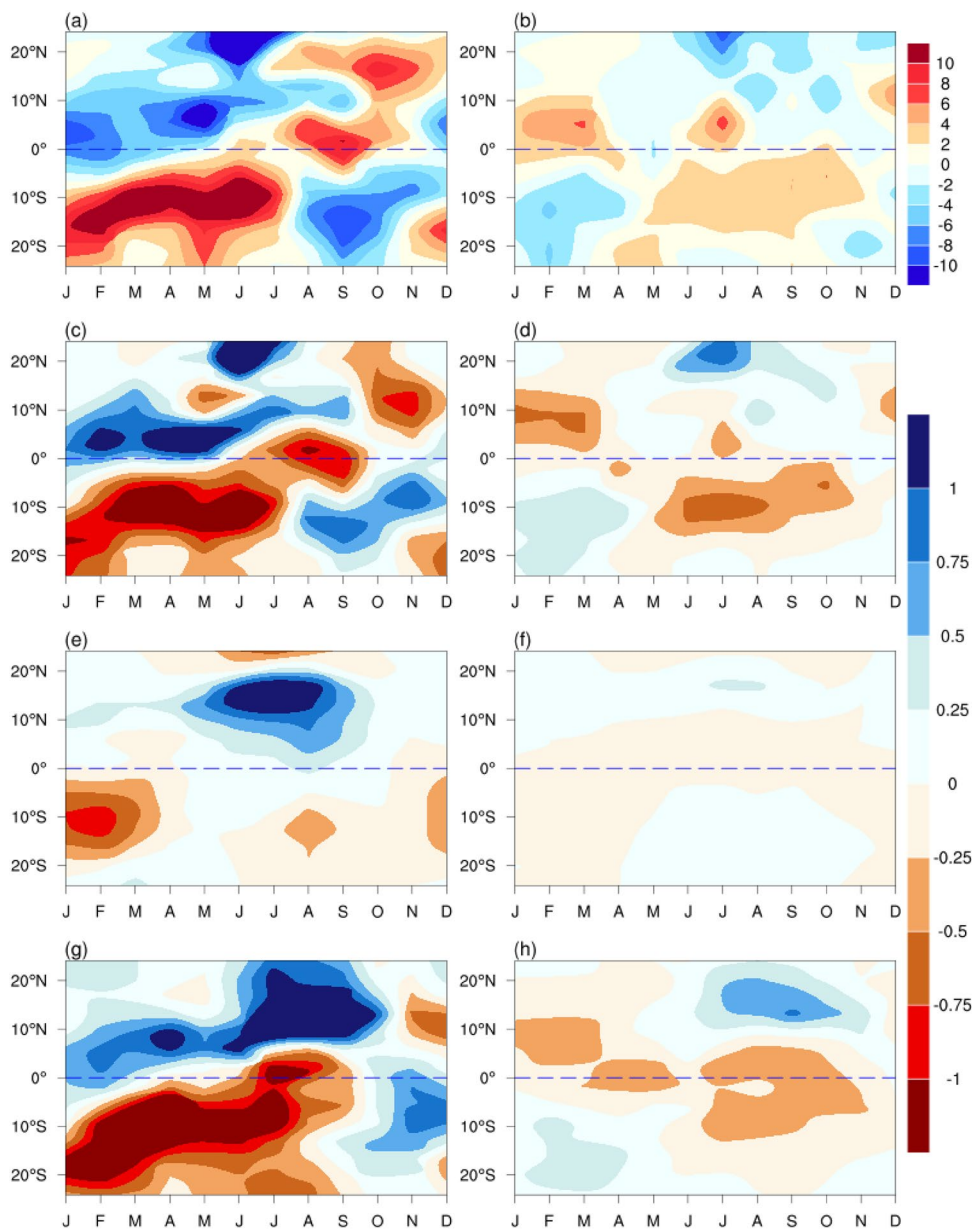


**Fig. 13** Circulation change and decomposition of precipitation change in response to precession (left panel) and obliquity (right panel) variations. **a** Pressure velocity at 500 hPa ( $10^{-3}$  Pa/s), **c** dynamic, **e** thermodynamic components and **g** total rainfall changes (mm/day)



and uncertain phase changes over ocean (Dwyer et al. 2014; Song et al. 2020).

Figure 12a and b show the leading EOF mode of seasonal variations of precipitation and SST in P0TL, which explains 65.6% and 89.4% of the variance, respectively. The P0TH-P0TL differences in PC1 is small (Fig. 12c and d), indicating no significant shift in the evolution of the seasonal cycle of both rainfall and SST in response to obliquity forcing. A similar result is obtained using the method in Song et al. (2018a) (not shown).

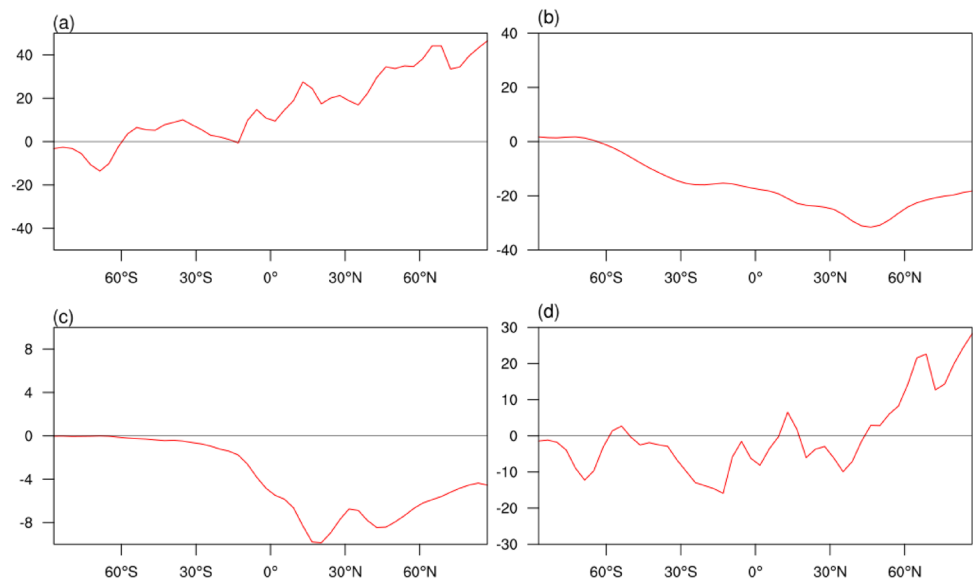
To understand the seasonal precipitation response, we decompose the tropical precipitation changes using Eq. (1) mentioned above. Figure 13c and e show the contribution of dynamic and thermodynamic terms under precession

forcing, with lateral advection and evaporation terms being neglected for their minor effects. The dynamic component (Fig. 13c) causes rainfall to increase in the transitional season (AMJ in the NH and OND in the SH), consistent with the vertical motion changes (Fig. 13a). The thermodynamic component is of minor importance except in the summer season (Fig. 13e). The water vapor budget method reproduces the precipitation changes well (Fig. 13g).

Figure 13d and f show the results of moisture budget under obliquity forcing (lateral advection and evaporation terms are neglected for their minor effects). The precipitation changes are mostly dominated by the dynamic component (Fig. 13d). The precipitation increases in summer, and decreases in winter in both hemispheres. However, the



**Fig. 14** The difference in atmospheric energy changes ( $\text{W/m}^2$ ) between AMJ and JAS in response to precession forcing. **a** Net input energy, **b** vertically integrated negative moist static energy tendency, **c** vertically integrated negative latent energy tendency, and **d** the sum of **(a)** and **(b)**



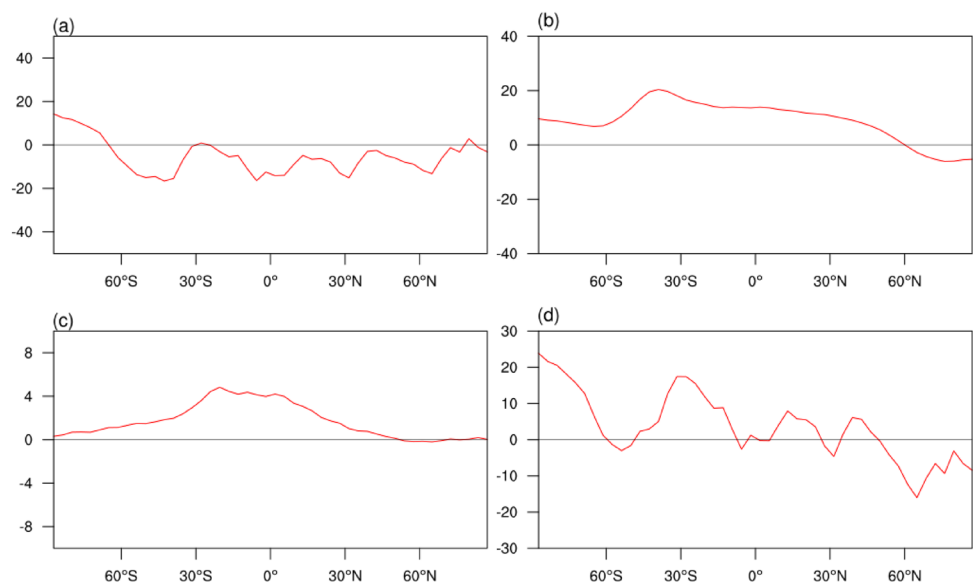
dynamic effect in the transitional seasons is small, consistent with the vertical motion changes (Fig. 13b). The thermodynamic component only makes a minor contribution to the overall rainfall changes (Fig. 13f). The water vapor budget method reproduces the precipitation changes well (Fig. 13h).

When the perihelion varies from December to June, the seasonal difference in the changes of  $F_{net}$  between AMJ and JAS has strong interhemispheric contrast (Fig. 14a), with the NH  $20.5 \text{ W/m}^2$  higher than the SH. Furthermore, the seasonal difference in the changes of negative moist static energy tendency shows a strong interhemispheric contrast as well, but with the NH  $12.9 \text{ W/m}^2$  lower than the SH (Fig. 14b). Further decomposition of  $h$  indicates that the seasonal difference in the changes of negative latent energy tendency,  $-\frac{\partial(L_v q)}{\partial t}$  (Fig. 14c), has a similar pattern to

that of the negative moist static energy tendency but shows a much smaller magnitude. The combined effects of net input energy and moist static energy tendency (Fig. 14d) induce a southward cross-equatorial energy transport for energy balance.

Previous studies suggested that a southward cross-equatorial energy transport corresponds to a northward shift of tropical precipitation, and vice versa (Kang et al. 2008; Schneider et al. 2014). However, the cross-equatorial energy transport during OND is dominated by the moist static energy tendency, with  $F_{net}$  showing a small interhemispheric contrast (Fig. 15a, b). The resulting northward cross-equatorial energy transport corresponds to a southward shift of tropical precipitation, hence resulting in

**Fig. 15** Same as Fig. 14 but for difference between OND and JFM



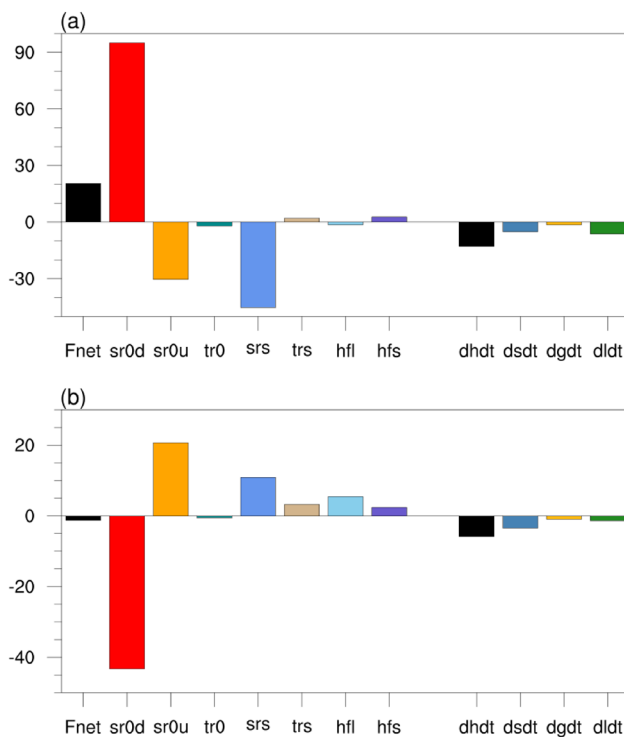


**Fig. 16** The interhemispheric energy contrast ( $\text{W/m}^2$ ) for the difference in  $F_{\text{net}}$  ( $F_{\text{net}}$ ) and  $-\frac{\partial(h)}{\partial t}$  ( $dhdt$ ) (a) between AMJ and JAS, and (b) between OND and JFM in response to precession forcing, and the contributions from  $S_t^{\downarrow}$  ( $sr0d$ ),  $-S_t^{\uparrow}$  ( $sr0u$ ),  $-R_t^{\uparrow}$  ( $tr0$ ), net solar radiation at surface ( $srs$ ), net longwave radiation at surface ( $trs$ ), LH ( $hfl$ ), SH ( $hfs$ ),  $-\frac{\partial(c_p T)}{\partial t}$  ( $dsdt$ ),  $-\frac{\partial(gz)}{\partial t}$  ( $dgdt$ ) and  $-\frac{\partial(L_v q)}{\partial t}$  ( $dldt$ )

a seasonal advance in the migration of tropical precipitation from the NH to the SH.

Figure 16 shows the contributions from different components of  $F_{\text{net}}$  and  $-\frac{\partial(h)}{\partial t}$  to the interhemispheric energy contrast for the difference between AMJ and JAS shown in Fig. 14 and the difference between OND and JFM shown in Fig. 15. The  $F_{\text{net}}$  term is dominated by the incoming shortwave radiation at the top of atmosphere, while  $-\frac{\partial(L_v q)}{\partial t}$  ( $-\frac{\partial(c_p T)}{\partial t}$ ) accounts for a larger contribution to  $-\frac{\partial(h)}{\partial t}$  term between AMJ and JAS (between OND and JFM).

As with the precession change, the shift of tropical precipitation in response to obliquity forcing has been explored from an energetics perspective. The seasonal difference in the change of combined effects of net input energy and moist static energy tendency between AMJ and JAS (or OND and JFM) shows small interhemispheric contrast (figures not shown), indicating little cross-equatorial energy transport, consistent with the results described above.

## 5 Conclusions and discussion

The present study investigates the effect of precession and obliquity separately on the global monsoon. It is shown that the global monsoon is influenced by both precession and obliquity changes. During minimum precession, an increase in monsoon precipitation occurs over the NH monsoon regions, whereas most parts of the SH monsoons experience a decrease with respect to maximum precession. With high obliquity, monsoon precipitation during austral summer is reduced over the South American monsoon, opposite to the precipitation increase over the South African and Australian monsoon regions. The obliquity signal in JJA precipitation under the minimum precession is different from that of a circular Earth orbit and under the maximum precession. The monsoon precipitation responses to both precession and obliquity forcing are mostly dominated by the dynamic component. The northward extension of the North African summer monsoon is associated with the thermodynamic components both for decreased precession and increased obliquity.

With low precession, the seasonal cycle of tropical rainfall is advanced, and the monsoon period shortens in the NH and lengthens in the SH. The rainfall increase in the transitional season is dominated by the dynamic component. From an energetics perspective, the combined effects of net input energy and moist static energy tendency induce a southward (northward) cross-equatorial energy transport during April–June (October–December), corresponding to a northward (southward) shift of tropical precipitation, hence resulting in a seasonal advance in the migration of tropical precipitation. However, there is no significant seasonal cycle change under obliquity forcing.

Some sediment records retrieved in the Asian monsoon region (Morley and Heusser 1997; Sun et al. 2006) show large phase differences with NH summer insolation, while Chinese speleothems present a synchronous variation (Cheng et al. 2012b; Wang et al. 2008). Shi et al. (2016) suggested that when the local summer insolation is weaker, the longer duration can counterbalance the reduced monsoon intensity and results in larger integrated precipitation amount over northern China, India and Indo-china peninsula. In present study, however, a consistent spatial pattern between annual precipitation, which include the influence of monsoon duration, and JJA precipitation is found over all of the six regional monsoon areas (Asia, North and South Africa, Australia, North and South America) (not shown). In their analysis, Shi et al. (2016) neglected possible oceanic feedbacks, which has been found to play an important role in Asian monsoon (Liu et al. 2003). This may be the reason for the different precipitation responses. Further modeling experiments are needed to investigate the relative roles of the

direct insolation forcing and ocean patterns in the responses of global monsoon duration to orbital forcing.

**Acknowledgements** We appreciate the comments of two anonymous reviewers that help the improvement of this study. This work was supported by the National Natural Science Foundation of China (41831175, 91937302 and 41721004), STEP(2019QZKK0102), Key Deployment Project of Centre for Ocean Mega-Research of Science, Chinese Academy of Sciences (COMS2019Q03), the Strategic Priority Research Program of Chinese Academy of Sciences (XDA20060501), and the National Key R&D Program of China (2018YFA0605904).

## References

- Ashkenazy Y, Eisenman I, Gildor H, Tziperman E (2010) The effect of Milankovitch variations in insolation on equatorial seasonality. *J Clim* 23:6133–6142. <https://doi.org/10.1175/2010jcli3700.1>
- Berger AL (1978) Long-term variations of daily insolation and Quaternary climatic changes. *J Atmos Sci* 35:2362–2367. [https://doi.org/10.1175/1520-0469\(1978\)035%3c2362:Ltvodi%3e2.0.Co;2](https://doi.org/10.1175/1520-0469(1978)035%3c2362:Ltvodi%3e2.0.Co;2)
- Biasutti M, Sobel AH (2009) Delayed Sahel rainfall and global seasonal cycle in a warmer climate. *Geophys Res Lett* 36:L23707. <https://doi.org/10.1029/2009gl041303>
- Bosmans JHC, Drijfhout SS, Tuenter E, Hilgen FJ, Lourens LJ (2015a) Response of the North African summer monsoon to precession and obliquity forcings in the EC-Earth GCM. *Clim Dyn* 44:279–297. <https://doi.org/10.1007/s00382-014-2260-z>
- Bosmans JHC, Hilgen FJ, Tuenter E, Lourens LJ (2015b) Obliquity forcing of low-latitude climate. *Clim Past* 11:1335–1346. <https://doi.org/10.5194/cp-11-1335-2015>
- Bosmans JHC et al (2018) Response of the Asian summer monsoons to idealized precession and obliquity forcing in a set of GCMs. *Quatern Sci Rev* 188:121–135. <https://doi.org/10.1016/j.quascirev.2018.03.025>
- Caley T et al (2011) Orbital timing of the Indian, East Asian and African boreal monsoons and the concept of a ‘global monsoon.’ *Quatern Sci Rev* 30:3705–3715. <https://doi.org/10.1016/j.quascirev.2011.09.015>
- Caley T, Roche DM, Renssen H (2014) Orbital Asian summer monsoon dynamics revealed using an isotope-enabled global climate model. *Nat Commun* 5:5371. <https://doi.org/10.1038/ncomms6371>
- Chen G-S, Liu Z, Clemens SC, Prell WL, Liu X (2011) Modeling the time-dependent response of the Asian summer monsoon to obliquity forcing in a coupled GCM: a PHASEMAP sensitivity experiment. *Clim Dyn* 36:695–710. <https://doi.org/10.1007/s00382-010-0740-3>
- Cheng H, Sinha A, Wang X, Cruz FW, Edwards RL (2012a) The Global Paleomonsoon as seen through speleothem records from Asia and the Americas. *Clim Dyn* 39:1045–1062. <https://doi.org/10.1007/s00382-012-1363-7>
- Cheng H et al (2012b) The climatic cyclicity in semiarid-arid central Asia over the past 500,000 years. *Geophys Res Lett*. <https://doi.org/10.1029/2011gl050202>
- Chou C, Neelin JD, Chen C-A, Tu J-Y (2009) Evaluating the “rich-get-richer” mechanism in tropical precipitation change under global warming.” *J Clim* 22:1982–2005. <https://doi.org/10.1175/2008jcli2471.1>
- Clemens SC, Prell WL, Sun Y (2010) Orbital-scale timing and mechanisms driving Late Pleistocene Indo-Asian summer monsoons: Reinterpreting cave speleothem  $\delta^{18}\text{O}$ . *Paleoceanography* 25:PA4207. <https://doi.org/10.1029/2010pa001926>
- Clement AC, Hall A, Broccoli AJ (2004) The importance of precessional signals in the tropical climate. *Clim Dyn* 22:327–341. <https://doi.org/10.1007/s00382-003-0375-8>
- deMenocal P, Ortiz J, Guilderson T, Adkins J, Sarnthein M, Baker L, Yarusinsky M (2000) Abrupt onset and termination of the African Humid Period: rapid climate responses to gradual insolation forcing. *Quatern Sci Rev* 19:347–361. [https://doi.org/10.1016/s0277-3791\(99\)00081-5](https://doi.org/10.1016/s0277-3791(99)00081-5)
- Ding Z, Huang G, Wang P, Qu X (2017) Last millennium climate simulated by the ICM climate model (in Chinese). *Clim Environ Res* 22(6):717–732. <https://doi.org/10.3878/j.issn.1006-9558.2017.16208>
- Dwyer JG, Biasutti M, Sobel AH (2014) The effect of greenhouse gas-induced changes in SST on the annual cycle of zonal mean tropical precipitation. *J Clim* 27(12):4544–4565
- Erb MP, Broccoli AJ, Clement AC (2013) The contribution of radiative feedbacks to orbitally driven climate change. *J Clim* 26:5897–5914. <https://doi.org/10.1175/jcli-d-12-00419.1>
- Gupta AK, Anderson DM, Pandey DN, Singhvi AK (2006) Adaptation and human migration, and evidence of agriculture coincident with changes in the Indian summer monsoon during the Holocene. *Curr Sci* 90(8):1082–1090
- Hsu Y-H, Chou C, Wei K-Y (2010) Land-ocean asymmetry of tropical precipitation changes in the mid-Holocene. *J Clim* 23:4133–4151. <https://doi.org/10.1175/2010jcli3392.1>
- Huang P, Wang P, Hu K, Huang G, Zhang Z, Liu Y, Yan B (2014) An introduction to the integrated climate model of the center for monsoon system research and its simulated influence of El Niño on East Asian-Western North Pacific climate. *Adv Atmos Sci* 31:1136–1146. <https://doi.org/10.1007/s00376-014-3233-1>
- Joussaume S, Braconnot P (1997) Sensitivity of paleoclimate simulation results to the season definitions. *J Geophys Res* 102:1943–1956
- Joussaume S et al (1999) Monsoon changes for 6000 years ago: results of 18 simulations from the Paleoclimate Modeling Intercomparison Project (PMIP). *Geophys Res Lett* 26:859–862. <https://doi.org/10.1029/1999gl1900126>
- Kang SM, Held IM, Frierson DMW, Zhao M (2008) The response of the ITCZ to extratropical thermal forcing: Idealized slab-ocean experiments with a GCM. *J Clim* 21:3521–3532. <https://doi.org/10.1175/2007jcli2146.1>
- Kershaw AP, van der Kaars S, Moss PT (2003) Late Quaternary Milankovitch-scale climatic change and variability and its impact on monsoonal Australasia. *Mar Geol* 201:81–95. [https://doi.org/10.1016/s0025-3227\(03\)00210-x](https://doi.org/10.1016/s0025-3227(03)00210-x)
- Khon VC, Park W, Latif M, Mokhov II, Schneider B (2010) Response of the hydrological cycle to orbital and greenhouse gas forcing. *Geophys Res Lett*. <https://doi.org/10.1029/2010gl044377>
- Kohfeld KE, Harrison SP (2000) How well can we simulate past climates? Evaluating the models using global palaeoenvironmental datasets. *Quatern Sci Rev* 19:321–346. [https://doi.org/10.1016/s0277-3791\(99\)00068-2](https://doi.org/10.1016/s0277-3791(99)00068-2)
- Kutzbach JE, Liu X, Liu Z, Chen G (2008) Simulation of the evolutionary response of global summer monsoons to orbital forcing over the past 280,000 years. *Clim Dyn* 30:567–579. <https://doi.org/10.1007/s00382-007-0308-z>
- Lee J-E, Fox-Kemper B, Horvat C, Ming Y (2019) The response of East Asian monsoon to the precessional cycle: a new study using the geophysical fluid dynamics laboratory model. *Geophys Res Lett* 46:11388–11396. <https://doi.org/10.1029/2019gl082661>
- Liu TS, Ding ZL, Rutter N (1999) Comparison of Milankovitch periods between continental loess and deep sea records over the last 2.5 Ma. *Quatern Sci Rev* 18:1205–1212. [https://doi.org/10.1016/s0277-3791\(98\)00110-3](https://doi.org/10.1016/s0277-3791(98)00110-3)
- Liu Z, Otto-Bliessner B, Kutzbach J, Li L, Shields C (2003) Coupled climate simulation of the evolution of global monsoons in the



- Holocene. *J Clim* 16:2472–2490. [https://doi.org/10.1175/1520-0442\(2003\)016%3c2472:Ccsote%3e2.0.Co;2](https://doi.org/10.1175/1520-0442(2003)016%3c2472:Ccsote%3e2.0.Co;2)
- Liu X, Liu Z, Kutzbach JE, Clemens SC, Prell WL (2006) Hemispheric insolation forcing of the Indian Ocean and Asian monsoon: local versus remote impacts. *J Clim* 19:6195–6208. <https://doi.org/10.1175/jcli3965.1>
- Liu B, Zhao G, Huang G, Wang P, Yan B (2017) The dependence on atmospheric resolution of ENSO and related East Asian-western North Pacific summer climate variability in a coupled model. *Theoret Appl Climatol* 133:1207–1217. <https://doi.org/10.1007/s00704-017-2254-y>
- Lourens LJ, Wehausen R, Brumsack HJ (2001) Geological constraints on tidal dissipation and dynamical ellipticity of the Earth over the past three million years. *Nature* 409:1029–1033. <https://doi.org/10.1038/35059062>
- Madec G (2008) NEMO ocean engine. Note du Pole de modélisation. Institut Pierre-Simon Laplace (IPSL), France, pp 1288–1619
- Mantsis DF, Clement AC, Kirtman B, Broccoli AJ, Erb MP (2013) Precessional cycles and their influence on the North Pacific and North Atlantic summer anticyclones. *J Clim* 26:4596–4611. <https://doi.org/10.1175/jcli-d-12-00343.1>
- Mantsis DF, Lintner BR, Broccoli AJ, Erb MP, Clement AC, Park H-S (2014) The response of large-scale circulation to obliquity-induced changes in meridional heating gradients. *J Clim* 27:5504–5516. <https://doi.org/10.1175/jcli-d-13-00526.1>
- Merlis TM, Schneider T, Bordoni S, Eisenman I (2013a) Hadley circulation response to orbital precession Part I: Aquaplanets. *J Clim* 26:740–753. <https://doi.org/10.1175/jcli-d-11-00716.1>
- Merlis TM, Schneider T, Bordoni S, Eisenman I (2013b) Hadley circulation response to orbital precession. Part II: Subtropical continent. *J Clim* 26:754–771. <https://doi.org/10.1175/jcli-d-12-00149.1>
- Mohtadi M, Prange M, Steinke S (2016) Palaeoclimatic insights into forcing and response of monsoon rainfall. *Nature* 533:191–199. <https://doi.org/10.1038/nature17450>
- Morley JJ, Heusser LE (1997) Role of orbital forcing in east Asian monsoon climates during the last 350 kyr: evidence from terrestrial and marine climate proxies from core RC14-99. *Paleoceanography* 12:483–493. <https://doi.org/10.1029/97pa00213>
- Neelin JD, Held IM (1987) Modeling tropical convergence based on the moist static energy budget. *Mon Weather Rev* 115:3–12. [https://doi.org/10.1175/1520-0493\(1987\)115%3c0003:Mtcbot%3e2.0.Co;2](https://doi.org/10.1175/1520-0493(1987)115%3c0003:Mtcbot%3e2.0.Co;2)
- Pokras EM, Mix AC (1987) Earth's precessional cycle and Quaternary climatic change in tropical Africa. *Nature* 326:486–487
- Pollard D, Reusch DB (2002) A calendar conversion method for monthly mean paleoclimate model output with orbital forcing. *J Geophys Res* 107:4615. <https://doi.org/10.1029/2002JD002126>
- Prell WL, Kutzbach JE (1987) Monsoon variability over the past 150000 years. *J Geophys Res* 92:8411–8425. <https://doi.org/10.1029/JD092iD07p08411>
- Roeckner E et al (2003) The atmospheric general circulation model ECHAM5. PART1: Model description. Report 349. Max Planck Institute for Meteorology, Hamburg, p 140
- Rossignol-Strick M (1983) African monsoons, an immediate climate response to orbital insolation. *Nature* 304:46–49. <https://doi.org/10.1038/304046a0>
- Schneider T, Bischoff T, Haug GH (2014) Migrations and dynamics of the intertropical convergence zone. *Nature* 513:45–53. <https://doi.org/10.1038/nature13636>
- Seth A, Rauscher SA, Biasutti M, Giannini A, Camargo SJ, Rojas M (2013) CMIP5 projected changes in the annual cycle of precipitation in monsoon regions. *J Clim* 26:7328–7351. <https://doi.org/10.1175/jcli-d-12-00726.1>
- Shi Z (2016) Response of Asian summer monsoon duration to orbital forcing under glacial and interglacial conditions: Implication for precipitation variability in geological records. *Quatern Sci Rev* 139:30–42. <https://doi.org/10.1016/j.quascirev.2016.03.008>
- Shi Z, Liu X, Sun Y, An Z, Liu Z, Kutzbach J (2011) Distinct responses of East Asian summer and winter monsoons to astronomical forcing. *Clim Past* 7:1363–1370. <https://doi.org/10.5194/cp-7-1363-2011>
- Shi Z, Liu X, Cheng X (2012) Anti-phased response of northern and southern East Asian summer precipitation to ENSO modulation of orbital forcing. *Quatern Sci Rev* 40:30–38. <https://doi.org/10.1016/j.quascirev.2012.02.019>
- Song F, Leung LR, Lu J, Dong L (2018a) Seasonally dependent responses of subtropical highs and tropical rainfall to anthropogenic warming. *Nat Clim Change* 8:787–792. <https://doi.org/10.1038/s41558-018-0244-4>
- Song F, Leung LR, Lu J, Dong L (2018b) Future changes in seasonality of the North Pacific and North Atlantic subtropical highs. *Geophys Res Lett* 45(21):11959–11968
- Song F, Lu J, Leung LR, Liu F (2020) Contrasting phase changes of precipitation annual cycle between land and ocean under global warming. *Geophys Res Lett*. <https://doi.org/10.1029/2020gl090327>
- Sun YB, Clemens SC, An ZS, Yu ZW (2006) Astronomical timescale and palaeoclimatic implication of stacked 3.6-Myr monsoon records from the Chinese Loess Plateau. *Quatern Sci Rev* 25:33–48. <https://doi.org/10.1016/j.quascirev.2005.07.005>
- Tuenter E, Weber SL, Hilgen FJ, Lourens LJ (2003) The response of the African summer monsoon to remote and local forcing due to precession and obliquity. *Global Planet Change* 36:219–235
- Valcke S (2006) OASIS3 user guide. PRISM Tech Rep 3:64
- Wang B, Ding Q (2008) Global monsoon: dominant mode of annual variation in the tropics. *Dyn Atmos Oceans* 44:165–183. <https://doi.org/10.1016/j.dynatmoce.2007.05.002>
- Wang Y et al (2008) Millennial- and orbital-scale changes in the East Asian monsoon over the past 224,000 years. *Nature* 451:1090–1093. <https://doi.org/10.1038/nature06692>
- Wang B, Liu J, Kim H-J, Webster PJ, Yim S-Y (2012) Recent change of the global monsoon precipitation (1979–2008). *Clim Dyn* 39:1123–1135. <https://doi.org/10.1007/s00382-011-1266-z>
- Wang PX, Wang B, Cheng H, Fasullo J, Guo ZT, Kiefer T, Liu ZY (2014) The global monsoon across timescales: coherent variability of regional monsoons. *Clim Past* 10:2007–2052. <https://doi.org/10.5194/cp-10-2007-2014>
- Weber SL, Tuenter E (2011) The impact of varying ice sheets and greenhouse gases on the intensity and timing of boreal summer monsoons. *Quatern Sci Rev* 30:469–479. <https://doi.org/10.1016/j.quascirev.2010.12.009>
- Wu C-H, Lee S-Y, Chiang JCH, Hsu H-H (2016) The influence of obliquity in the early Holocene Asian summer monsoon. *Geophys Res Lett* 43:4524–4530. <https://doi.org/10.1002/2016gl068481>
- Wyrwoll K-H, Liu Z, Chen G, Kutzbach JE, Liu X (2007) Sensitivity of the Australian summer monsoon to tilt and precession forcing. *Quatern Sci Rev* 26:3043–3057. <https://doi.org/10.1016/j.quascirev.2007.06.026>
- Xie P, Arkin PA (1997) Global precipitation: A 17-year monthly analysis based on gauge observations, satellite estimates. *Bull Am Meteorol Soc* 78:2539–2558